

pubs.acs.org/NanoLett Letter

Illuminating Invisible Grain Boundaries in Coalesced Single-Orientation WS₂ Monolayer Films

Danielle Reifsnyder Hickey, Nadire Nayir, Mikhail Chubarov, Tanushree H. Choudhury, Saiphaneendra Bachu, Leixin Miao, Yuanxi Wang, Chenhao Qian, Vincent H. Crespi, Joan M. Redwing, Adri C. T. van Duin, and Nasim Alem*



Cite This: Nano Lett. 2021, 21, 6487-6495



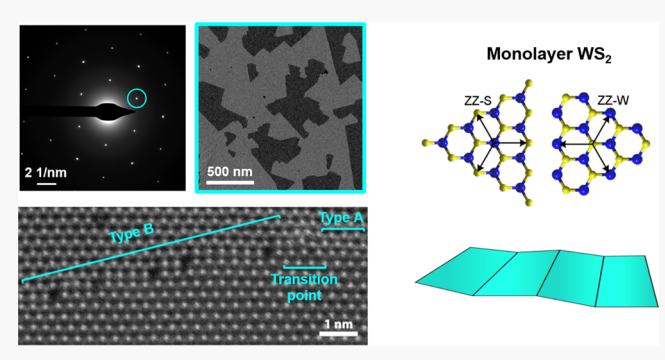
ACCESS

Metrics & More



s Supporting Information

ABSTRACT: Engineering atomic-scale defects is crucial for realizing wafer-scale, single-crystalline transition metal dichalcogenide monolayers for electronic devices. However, connecting atomic-scale defects to larger morphologies poses a significant challenge. Using electron microscopy and ReaxFF reactive force field-based molecular dynamics simulations, we provide insights into WS2 crystal growth mechanisms, providing a direct link between synthetic conditions and microstructure. Dark-field TEM imaging of coalesced monolayer WS2 films illuminates defect arrays that atomic-resolution STEM imaging identifies as translational grain boundaries. Electron diffraction and high-resolution imaging reveal that the films have nearly a single orientation with



imperfectly stitched domains that tilt out-of-plane when released from the substrate. Imaging and ReaxFF simulations uncover two types of translational mismatch, and we discuss their origin related to relatively fast growth rates. Statistical analysis of >1300 facets demonstrates that microstructural features are constructed from nanometer-scale building blocks, describing the system across sub-Ångstrom to multimicrometer length scales.

KEYWORDS: tungsten disulfide, transmission electron microscopy, chemical vapor deposition, grain boundaries, transition metal dichalcogenides, ReaxFF molecular dynamics

ransition metal dichalcogenides (TMDs) represent a frontier of semiconductor research due to their exciting optoelectronic properties and potential for integration into very thin devices. 1-9 However, incomplete understanding of how to achieve single-crystalline, device-scale films with minimal atomic-scale defects 10-12 has limited their performance. 13-16 To date, the materials properties of TMDs have been explored largely using isolated flakes that have either been exfoliated from bulk materials^{17–19} or grown by chemical and physical deposition techniques.^{20–22} Recently, growth of coalesced monolayer films on the wafer scale^{23–30} has been achieved by more controlled growth methods, such as metalorganic chemical vapor deposition (MOCVD), in which gasphase precursors provide increased tunability, and CVD enhanced by using multiple temperature zones. As achieving large-area monolayer films becomes possible, it is more critical to uncover defects that arise from synthesis, 31 such as grain boundaries (GBs) or point defects, and to understand the underlying physics behind their formation. With this understanding, we can further engineer defects and alleviate obstacles to single crystallinity.³²

Typically, islands of TMDs have triangular or hexagonal morphologies following the kinetic Wulff construction. 10,

This steady-state flake morphology can be described as a function of the thermodynamic conditions during synthesis, such as the chemical potentials of the elements involved, determined by precursor vapor pressures.40 Therefore, continuous epitaxial films resulting from the coalescence of orientationally aligned islands are also expected to exhibit facets along high-symmetry directions. Yet, the transmission electron microscopy (TEM) investigation presented here for monolayer 2H-WS2 films grown by MOCVD on 2 in. c-plane sapphire $[(0001) \alpha$ -Al₂O₃] substrates shows strikingly different GB structures compared to those arising from hexagonal symmetry.

Initial bright-field TEM imaging and selected-area electron diffraction (SAED) of the as-grown WS2 films that have been transferred from the growth substrate onto TEM grids show a

Received: April 17, 2021 Revised: June 3, 2021 Published: July 27, 2021





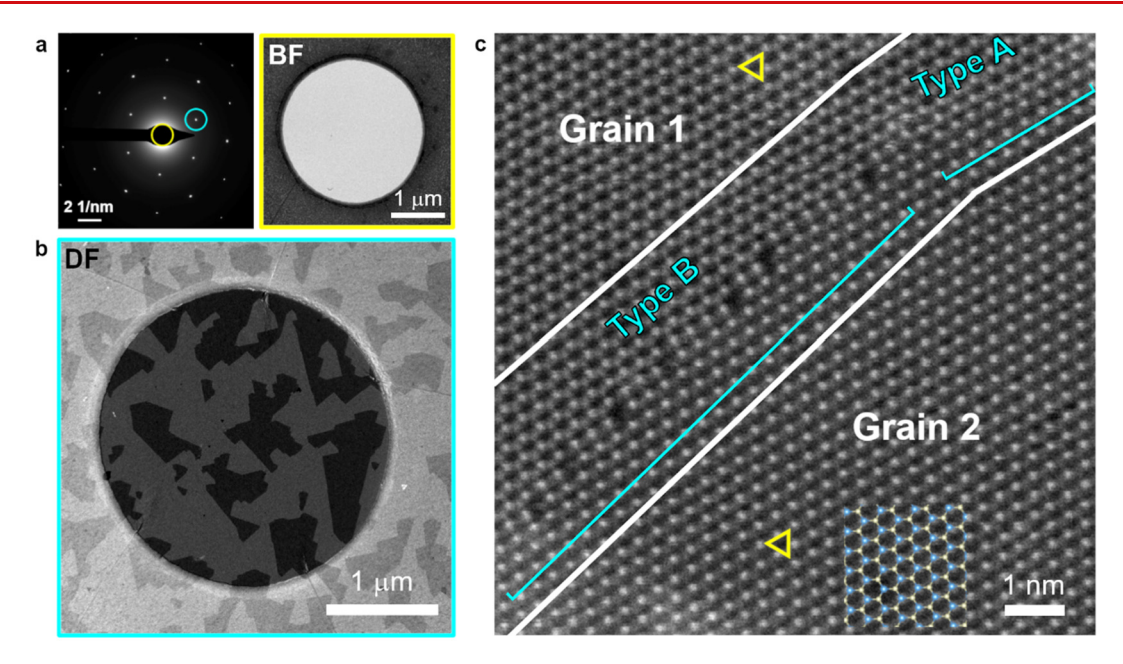


Figure 1. Structure of a nearly single-orientation monolayer 2H-WS $_2$ film and its GB defects. (a) SAED pattern (left) showing an apparently single-crystalline morphology, which corresponds to the featureless monolayer area shown in the BF-TEM image (right, created from the direct beam indicated by the yellow circle in the SAED pattern). The circle in the BF-TEM image represents the free-standing film area in a hole in the Quantifoil carbon TEM substrate. (b) DF-TEM image (created from the Bragg spot indicated by the cyan circle in (a)) of the area in the BF-TEM image in (a), showing irregular, faceted features in the monolayer. (c) Atomic-resolution ADF-STEM image of two similarly oriented grains meeting at a GB (in the atomic model, blue represents W and yellow represents S).

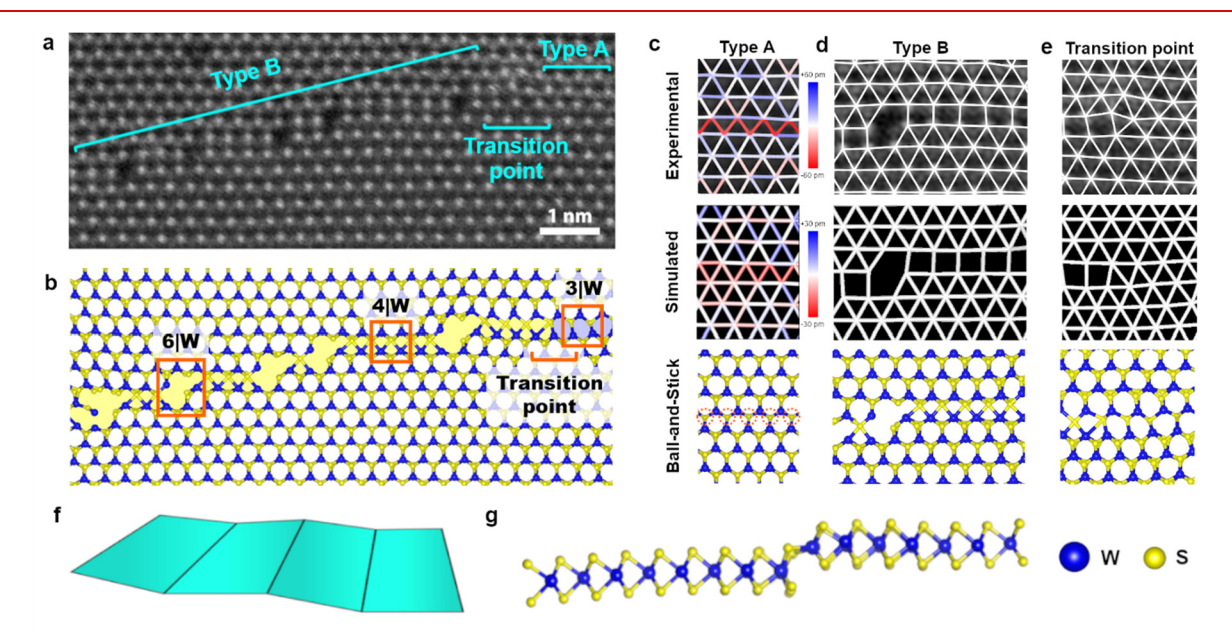


Figure 2. Local structures obtained from experimental ADF-STEM imaging and ReaxFF MD simulation. (a) ADF-STEM image showing type A and B GBs, as well as the transition point between them. (b) ReaxFF MD simulation equilibrated at 300 K of the structure shown in (a). (c–e) Comparison (experiment, simulation, and ball-and-stick atomic model) of the grain boundary structures between adjacent epitaxial, oriented grains of WS₂: (c) type A mismatch, in which a single vacancy line results in compression of the planes (red) but retains the hexagonal arrangement (3lW) of metal atoms; (d) type B mismatch, in which a subunit-cell offset between the grains results in a rectangular arrangement (4lW) of metal atoms at the GB; and (e) the transition point between GB regions with 3lW and 4lW. Each dashed orange circle on the ball-and-stick model in (c) represents an S vacancy. (f) Representation of the low-angle tilt induced in the grains of the coalesced film upon release from the substrate. (g) Cross-sectional view of the ReaxFF MD simulated model of the freestanding type B GB, showing the out-of-plane tilt and abrupt atomic displacement at the GB.

uniform and featureless nearly single-crystalline film across multimicrometer regions (Figure 1a). This is consistent with the results of atomic force microscopy (AFM) and in-plane X-ray diffraction (XRD) that probe larger length scales and

support the monolayer thickness and large-area, millimeter-scale epitaxial nature of the WS_2 grown on sapphire.²⁹ The monolayer thickness is also verified via SAED tilt series^{41,42} from -15° to $+15^{\circ}$ and annular dark-field (ADF-) STEM

intensity line profiles (Figures S1 and S2). However, new features are uncovered when using dark-field (DF-) TEM imaging. We observe unexpected, irregular, linear defects throughout the several-micrometer squared areas of the almost epitaxial monolayer film that possesses a nearly single-crystalline diffraction pattern (Figure 1b). DF-TEM imaging further uncovers that the monolayer consists of two types of submicrometer squared regions, shown in two shades of gray.

Further inspection via atomic-resolution ADF-STEM imaging (Figure 1c) reveals that two neighboring WS₂ grains (dissimilar contrast in DF-TEM imaging) both retain the 2H structure and identical in-plane crystallographic orientation across the GB. Despite the SAED pattern appearing nearly single crystalline, the atomic-resolution imaging of the interface between regions with dissimilar DF-TEM contrast shows that these WS₂ films contain distinct GB atomic structures. Strikingly, no in-plane rotation of the grains occurs at this GB (confirmed by atomic imaging in Figure 1c and SAED in Figure 1a), and the WS₂ lattice orientation is nearly identical on both sides of the GB (marked by sulfur column triangles on Figure 1c). Instead, we observe single-orientation 2H grains that are stitched together at irregular, faceted angles that do not adopt the characteristic TMD island shapes with hexagonal symmetry. Impurities are also ruled out by compositional analysis (Figure S3). High-resolution ADF-STEM imaging of the GBs indicates a subunit cell translational disregistry (either transverse or longitudinal) between epitaxially oriented grains, with no observed in-plane misorientation. This leads to unexpected defect arrays throughout the film.

The widespread GB defect structures in Figure 1 (see also Figure S4) represent regions where monolayer islands have coalesced with two different types of mismatch along these boundaries (Figure 2). In the first case (type A), a translational GB is created when the hexagonal lattice is compressed perpendicular to the GB, resulting in decreased metal-to-metal distances while approximately retaining the in-plane hexagonal symmetry (3IW) of the grain interiors (Figure 2a-c) and creating compressive strain (Figure 2c). In the second case (type B), a translational GB is created when the hexagonal lattices meeting at the GB undergo a subunit-cell shift parallel to the GB, leading to transverse lattice disregistry (Figure 2a,b,d). This transverse disregistry leads to broken in-plane hexagonal symmetry, forming through shear a rectangular arrangement of tungsten atoms (4IW) connected by sulfur atoms along the GB.

ReaxFF reactive force field molecular dynamics (MD) simulations, depicted and compared with experiment in Figure 2b—e, support the formation of type A and B GB structures. ReaxFF, developed for a wide range of materials, including 2D materials, ^{43–45} enables large-scale (>1000 atoms) simulations on material chemistry. Specifically, the type A structure forms with sulfur vacancies along the GB. For this, sulfur vacancies (removal of one S atom at a 2S sublattice site) assemble into a single vacancy line defect (Figure 2c). The three undercoordinated W atoms surrounding every S vacancy relax toward the single-S atom columns, compressing the W–W distance projections across the type A GBs. Structurally, type A resembles compression lines formed in TMDs under highenergy electron beams, ^{46–48} but here they originate from the subunit-cell offset present during coalescence (Figure S5).

In contrast to type A, the type B GB (Figure 2d) does not contain S vacancies but instead occurs where two growing WS₂ grains contain subunit-cell mismatch parallel to the GB,

making it challenging for the grains to stitch together seamlessly. Therefore, the hexagonal symmetry is broken, and the type B GB adopts a rectangular arrangement of W atoms (4IW) along the boundary to account for the mismatch. Type B segments also contain 6IW rings that create steps along the length of the GB. In type B regions, the mismatched lattices adopt a structure more akin to an extended one-dimensional defect or "translational grain boundary", related to those previously reported in graphene. 49–51

We also experimentally observe transitions between type A and type B translational GBs indicating regions with both longitudinal and transverse shifts (Figure 2e). According to the MD simulations, the transition between type A and type B occurs when the 3lW ring (type A) evolves into the 4lW rectangular geometry (type B), associated with a relative shift between the grains parallel to the zigzag edge, by nearly half of the W–W bond distance ($\Delta L = d_{\rm w-w}/2 \approx 1.5$ Å), as well as a lattice distortion of ~0.1 Å perpendicular to the zigzag edge. This shift eliminates the longitudinal translational offset across the 4lW regions of the type B GB along the zigzag edge, and it fully transforms the type B GB into the type A with only transverse translational registry between the two grains. Importantly, the in-plane 2H lattice orientation remains identical across such boundaries in our experiments.

It is striking that the GBs connect grains that both possess the 2H structure, and yet, the contrast differences (both in DF-TEM, Figure 1b, and ADF-STEM, Figure 1c) suggest that they interact differently with the electron beam. We attribute this to residual offset during growth due to substrate interaction and subsequent tilt. The GBs occur where the in-plane oriented, coalescing grains stitch together imperfectly. As the film forms, many small nuclei merge, eventually forming the 2 in. waferscale film.²⁹ The c-plane sapphire substrate promotes van der Waals epitaxy but contains step edges and has lattice mismatch with WS₂. Therefore, translational registry cannot occur between a subset of the merging crystallites, creating distortion in the out-of-plane direction, while maintaining their orientation in the x-y plane. This leads to out-of-plane buckling of the film when it is released from the sapphire substrate and becomes a freestanding film on the TEM grid. Figure 2f,g represents this out-of-plane tilting of the grains with respect to each other and the abrupt atomic displacement at GBs, schematically and with a ReaxFF model, respectively.

To elucidate the origin of the observed DF-TEM contrast, we have measured the experimental DF-TEM image contrast ratio and compared it to the simulated diffraction peak intensity ratio for tilted WS₂ monolayers (Figures S6 and S7). We obtain quantitative agreement between the experimental DF-TEM ratio and simulated diffraction intensities for grains with a relative tilt angle of ~11°, although the exact tilt configuration throughout the film may vary according to the local GB structure, grain size, etc. Due to the unique nature of the GBs, further studies will be useful to accurately quantify multiple tilted regions, especially to examine effects such as the grain size and 6lW ring periodicity that contribute to longrange out-of-plane effects. To understand the tilted nature of the GBs, we have also modeled our structure as a 2H grain trapped within a 2H matrix, with the two grains connected by type B translational boundaries (Figure S8a,b). We have simulated ADF-STEM image intensities that are consistent with the maximum experimental ratio and support that the grains are tilted relative to each other. This correlation between measurements and modeling supports that tilt between grains

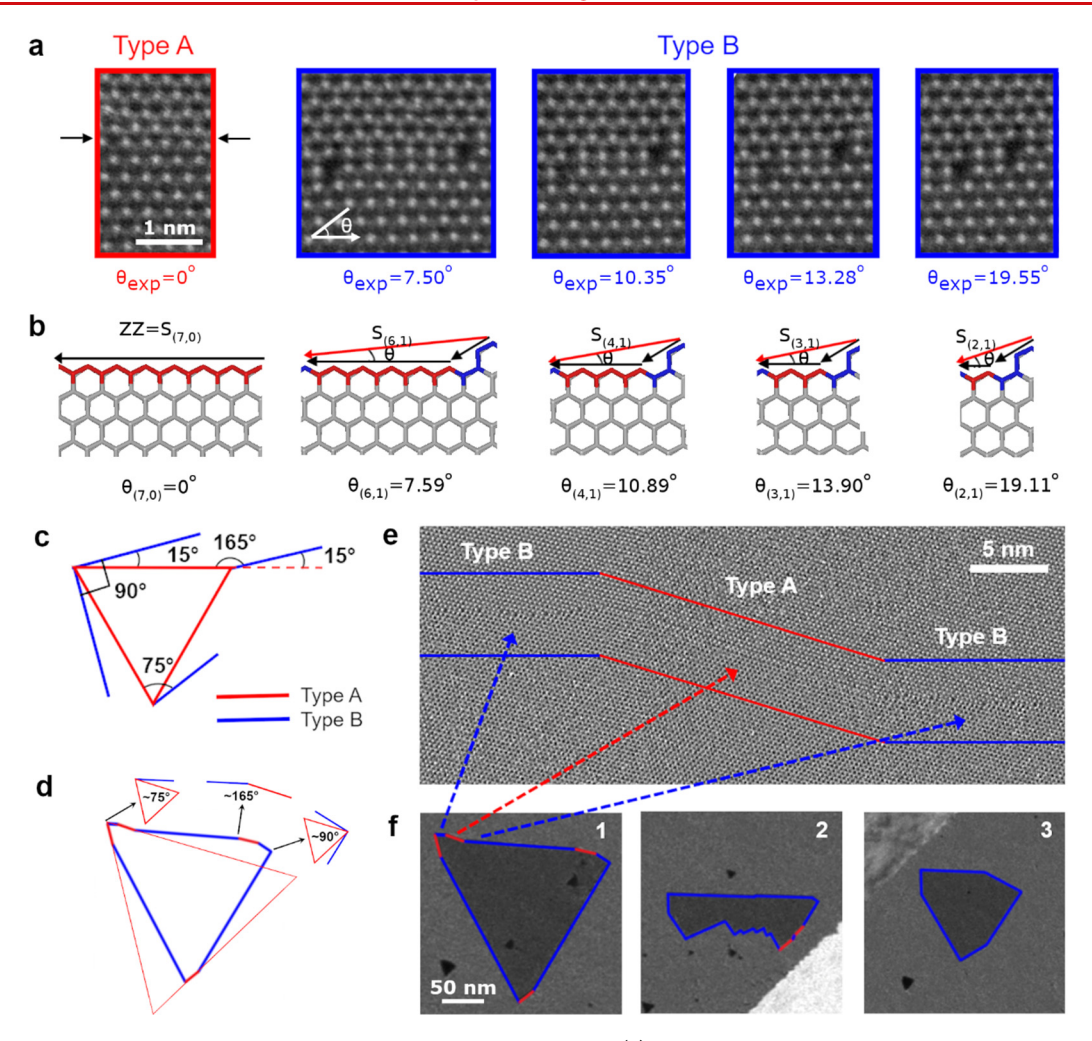


Figure 3. Correlation of atomic GB structures with facets observed via DF-TEM. (a) Experimental ADF-STEM images of the building block type A and B GB structures with the corresponding experimentally measured angles off the zigzag edge. (b) ReaxFF models corresponding to the images in (a), marked with the angle off the zigzag edge that a periodic stretch of this structure would create. (c) Schematic showing the regular hexagonal symmetry of the type A structure along the zigzag edge (red) and various angles that form from the average type B angle off the zigzag edge (\sim 15°) in combination with type A and type B orientations. (d) An overlay of the hexagonal symmetry of the zigzag edge (red triangle) and an experimentally observed configuration (blue and red polygon, in which the red regions coincide with the predicted zigzag edge and the blue regions are <20° off the zigzag edge). (e) Band-pass-filtered ADF-STEM image showing connections between three different facets that have type B—type A—type B atomic structures. The facets in this region consist of two boundary morphologies shown as red and blue facets in the DF-TEM image below. (f) Three examples of DF features with the GB facets marked in red or blue according to whether they are type A or type B.

explains why the translational GBs can be detected using DF-TEM imaging.

Previously, TMD monolayers have been reported to produce contrast differences in DF-TEM images when they either contain 60°-rotated grains connected by mirror twin boundaries⁵² or a phase transition between 2H and 1T TMD polymorphs.⁵³ We emphasize that neither is the case for our system (see Figures 1c, S9, and S11). In the WS2 monolayers studied here, the rotational mismatch between the two grains is negligible (Figure 1c), and therefore no mirror twin boundary is observed. We also rule out the presence of the 1T phase due to the distinct S columns visible on both sides of the GB in ADF-STEM imaging (Figure 1c), as well as the relative diffraction spot intensities and tilt behavior (Figures S1, S9), which are consistent with results from published, systematic comparisons of 2H and 1T diffraction. 42,54 Whereas the formation of mirror twinned regions and polymorphs has been a limiting factor for single-crystalline film growth, the films studied here possess a single orientation across numerous

multimicrometer squared areas sampled, despite the observed subtle defect array structures that represent coalescence of submicrometer-scale grains. This achievement underscores a remarkable step forward in large-scale TMD monolayer synthesis.²⁹

Despite the long-range geometrical irregularity of the regions identified by DF-TEM (Figure 1b), the GB structures described in Figure 2 provide a consistent explanation for the faceted features observed across multimicrometer squared areas. Figure 3 shows the correlation of DF-TEM facets with the atomic GB structures observed via ADF-STEM imaging (see also Figure S12). Here, the atomic building block registries lead to type A translational GBs (Figure 3a, red), which follow the zigzag edge of the 2H crystal structure, and type B "slanted" translational GBs (Figure 3a, blue), which deviate from the zigzag edge with stabilizing 6lW polygonal rings. Type B experimentally occurs (Figure 3a,b) with 6lW units occurring as infrequently as every sixth polygon (creating calculated angle $\theta_{6,1} = 7.59^{\circ}$ with the zigzag edge) and as

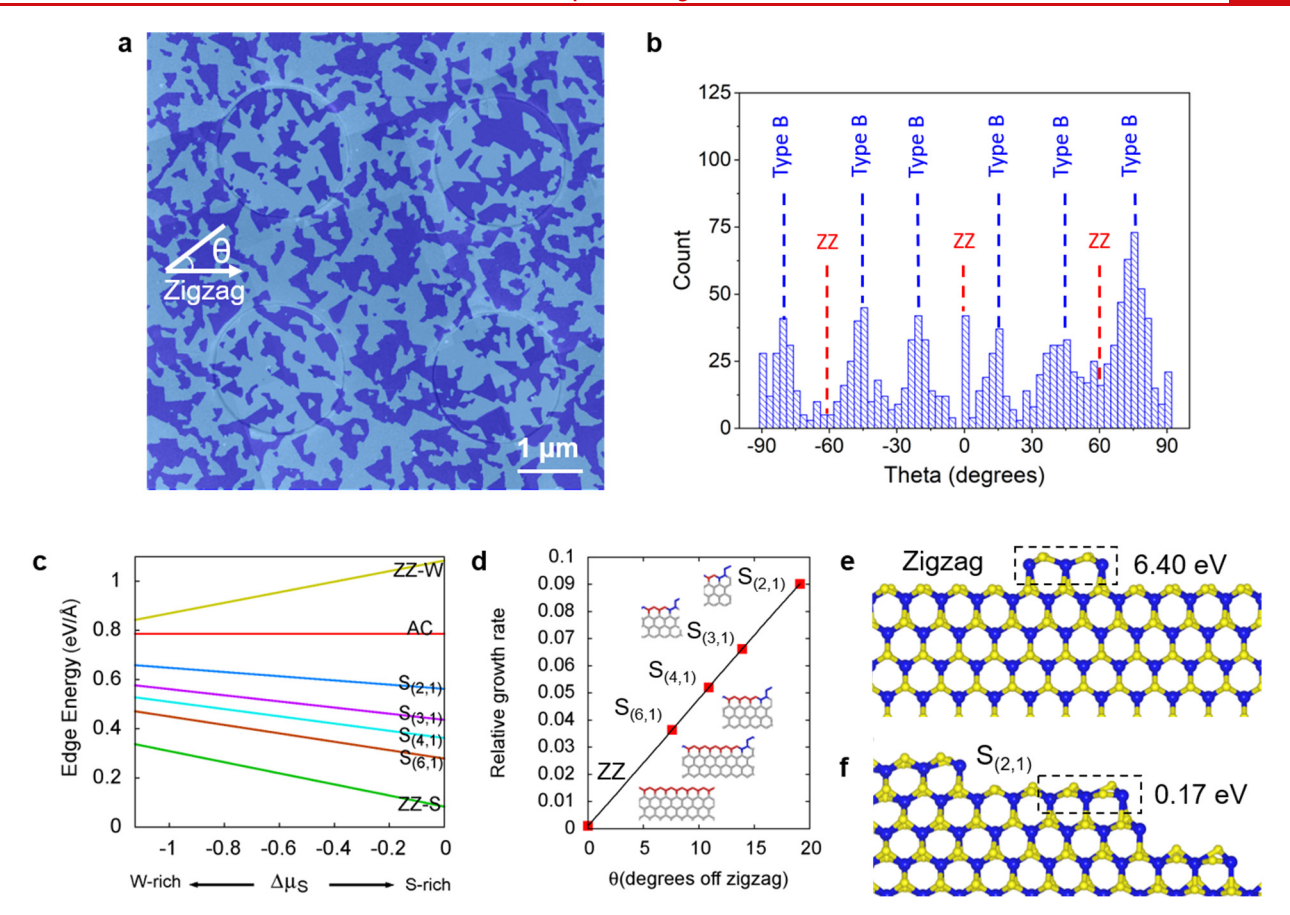


Figure 4. Distribution of GBs and energetics of GB formation. (a) Large-area false-colored composite DF-TEM map. (b) Histogram of facet orientations measured from the composite DF image in (a) (to reduce error, angles were only measured from free-standing film regions). Zigzag orientations are marked (present but a minor contribution), and type B orientations $\sim \pm 15^{\circ}$ off the zigzag dominate. (c) ReaxFF-calculated edge formation energies of S-zigzag (ZZ-S), slanted (S), armchair (AC), and W-zigzag (ZZ-W) edges as a function of the excess sulfur chemical potential, $\Delta \mu_{\rm S}$ (in eV). (d) Calculated relative growth rate of the slanted edge structures with respect to the ZZ-S edge as a function of slanted angle, θ. $S_{(2,1)}$, $S_{(3,1)}$, $S_{(4,1)}$, and $S_{(6,1)}$ are the slanted edges characterized by the translational vector (n, 1) of the 2H-WS₂ lattice, where n is the number of the zigzag units along the a_1 direction, and the a_2 -component vector contains only one zigzag unit in the GB of interest, as shown in Figure S11. (e, f) Illustrations of the formation energy for adding atoms (enclosed in the dashed rectangular boxes) onto the reference ZZ-S and $S_{(2,1)}$ slanted edges, respectively.

frequently as every second polygon ($\theta_{2,1}=19.11^\circ$), which creates the maximum possible angle away from the zigzag edge using the 4lW and 6lW components. Experimentally, the average slanted angle is ~15°, which indicates that type B primarily exists with combinations of the commonly observed $\theta_{2,1}=19.11^\circ$, $\theta_{3,1}=13.90^\circ$, and $\theta_{4,1}=10.89^\circ$. If we consider an average $\pm 15^\circ$ off the zigzag edge, multiple possible facet geometries emerge, several of which are illustrated in Figure 3c. Here, the 60° angles in the red triangle (an ideal flake) represent a standard TMD flake with the three zigzag edges that enclose an equilateral triangle. Blue lines represent facets at ~15° angles to their adjacent red zigzag edges. Further, combinations of these facets illustrate several experimentally observed angles, such as 75°, 165°, and 90°.

Figure 3d applies the illustration in Figure 3c to an experimentally observed DF-TEM image (shown in Figure 3f-1). Here, the red equilateral triangle represents the ideal type A boundary along the zigzag edge, and blue represents the slanted type B boundary. The experimentally obtained red and blue faceted polygon is positioned so the red facets are overlaid onto the equilateral triangle model. The experimental red facets clearly follow the modeled zigzag edges, and the blue facets create angles of $\sim 10^{\circ}-20^{\circ}$ with the red facets. Figure 3e

shows band-pass-filtered ADF-STEM imaging of two $\sim 165^\circ$ angles between the type B (blue) and the type A (red) facets. These facets correspond to the three indicated edges of DF feature 1 in Figure 3f-1, in which both red and blue facets are observed but blue facets are clearly more prevalent. Across numerous GBs analyzed (see also Figures S13 and S14), the type B (blue) structure dominates. Subsequently, the prevalence of blue type B facets clearly provides an explanation for the origin of the irregular GB angles that deviate from the regular $60^\circ/120^\circ$ symmetry expected for TMD flakes enclosed by zigzag edges.

In fact, large-area, composite DF-TEM mapping (Figure 4a) including >1300 facets shows the dominance of the irregularly oriented GBs. These boundaries possess an angular distribution (relative to the zigzag edge, as identified by ADF-STEM imaging; see Figure S14a) that peaks at type B orientations, i.e., $\sim 15^{\circ}$ off the zigzag edge (Figure 4b). This statistical analysis is consistent with local observations (e.g., Figure 3f) that the type B GB at $\sim 15^{\circ}$ off the zigzag direction is dominant. Nevertheless, a minority population does exist at 0° and 60° , which represents the observed type A GBs. The ReaxFF MD calculations of edge formation energies, computed as a function of the excess sulfur chemical potential, $\Delta \mu_{\rm S}$, by

eqs S1, S2, and S4, predict that the slanted edges lose their stability with increasing angle off the zigzag edge and associated kink (6lW) concentration (Figure 4c and eq S5). Additionally, as described in the literature, 55 a nearly linear relationship exists between the slanted angle and growth rate (Figure 4d and eqs S5-S7) that is determined by the formation energy (eq S6) necessary to add atoms onto a given edge (Figure 4e,f). In an S-rich environment such as studied here, the high energy cost of 6.40 eV required for the addition of the first zigzag unit (3W+4S atoms) onto the chalcogenterminated zigzag edge, ZZ-S, creates an obstacle to its growth (Figure 4e) because it is considerably larger than the thermal energy, $kT \sim 0.1$ eV at 1000 °C, as defined by the equation $R(\theta) \approx c_{ZZ}(\theta) e^{-6.40/kT}$ and reported in earlier work.⁵⁵ Therefore, although ZZ-S is the most stable edge structure, its growth rate is expected to be the slowest. In contrast, $S_{(2,1)}$, with a calculated angle of 19.1°, is determined to be less stable but to have the highest growth rate. This results from its negligible formation energy of 0.17 eV, required for the attachment of an extra zigzag unit (2W+4S atoms) to the 6lW kink of the S_(2,1) edge (Figure 4f), because it has the largest kink density considered (see the SI).

This analysis indicates that the growth of the ZZ-S edge requires near-equilibrium growth conditions and a long duration to complete its linear formation. This is consistent with simulations for graphene 56 and carbon nanotubes,5 which have established that their zigzag edges are more stable than edges 0° – 20° off the zigzag with growth rates related to the density of kinks. Therefore, for WS2, although the slanted edges are less stable and should disappear quickly during growth, kinetically controlled conditions may not allow flakes to complete their zigzag linear formation. Thus, grains with slanted edges may survive during the growth to meet at GBs, as observed in these films, aided by the limited distance between adjacent islands of WS₂ during growth. In fact, precedent exists in isolated flakes of graphene 55,58 and GaSe 59 for such slanted edges: in a series of growth-etching-regrowth studies, offzigzag edges (up to 19°) were preferentially observed as faster growing/etching edges than the zigzag edges. These related examples, however, did not have the spatial constraint of nearby islands during edge formation.

Figure 4c shows that the difference in the edge energies decreases as the system becomes W-rich. Whereas S-rich conditions thermodynamically favor zigzag edges (type A), intermediate or W-rich local conditions may promote the formation of slanted edges (type B). To produce a coalesced monolayer with minimal bilayer coverage, the WS2 analyzed here is synthesized in a multistep growth process. To achieve this, the temperature and metal precursor flux are controllably modulated over the course of the reaction.²⁹ This means that the growing film experiences multiple kinetic regimes and variable metal precursor concentrations. Whereas simulations indicate that type B edges grow quickly and would disappear in favor of zigzag edges if the reaction proceeded long enough, the growth conditions and resulting experimental observations clearly indicate that the film has a kinetically driven morphology. Also, the WS2 is grown in H2 ambient, which may promote competition between growth and etching when the W precursor flow rate is modulated. This may lead to trapping of the faster-growing, experimentally observed slanted edges (\sim 15°), even if they are not the fastest-growing edges predicted (19°). Therefore, adjusting the growth rate (by adjusting gas flow) and/or controlling the nucleation density

on the substrate could promote the disappearance of fast-growing, slanted edges and provide routes to reduce disregistry between growing WS₂ islands.

In summary, we have discovered translational defect arrays in nearly single-orientation, coalesced monolayer WS₂ films, and we have uncovered the origin of their apparently irregular faceting. By connecting the film microstructure across length scales (e.g., atomic structure to multimicrometer), we have created links that provide unexpected insights into the mechanism for crystal growth. Strikingly, we quantitatively characterize these irregular GBs to have specific, well-defined orientations off the zigzag edges due to their kinetically driven growth conditions. This investigation combined S/TEM imaging and ReaxFF MD simulations to uncover and quantify the relative orientations of GBs, demonstrating that these defect structures exist as subtle but widespread imperfections, despite growth conditions that produce nearly singleorientation, monolayer films. The defect arrays observed originate from grains coalescing without in-plane misorientation but with both in-plane subunit-cell translational (longitudinal and transverse) offsets and out-of-plane tilt between the two neighboring grains. Further engineering of growth processes can minimize this offset to produce singlecrystalline, wafer-scale, epitaxial, monolayer 2D TMD films with minimal defect arrays.

ASSOCIATED CONTENT

Solution Supporting Information

The Supporting Information is available free of charge at https://pubs.acs.org/doi/10.1021/acs.nanolett.1c01517.

Details of experimental methods and results, including synthesis, characterization, and modeling; additional characterization and simulation of features such as WS_2 thickness, tilt, and elemental composition; and examples of the coexistence of type A and B boundaries, the correlation between low-magnification DF-TEM imaging and atomic-resolution ADF-STEM imaging, and the process for measuring boundary orientations from DF-TEM maps and ADF-STEM imaging (PDF)

AUTHOR INFORMATION

Corresponding Author

Nasim Alem – Department of Materials Science and Engineering, The Pennsylvania State University, University Park, Pennsylvania 16802, United States; ⊚ orcid.org/0000-0003-0009-349X; Email: nua10@psu.edu

Authors

Danielle Reifsnyder Hickey — Department of Materials Science and Engineering, The Pennsylvania State University, University Park, Pennsylvania 16802, United States; orcid.org/0000-0002-8962-1473

Nadire Nayir — 2D Crystal Consortium-Materials Innovation Platform (2DCC-MIP), Materials Research Institute, The Pennsylvania State University, University Park, Pennsylvania 16802, United States; Department of Mechanical Engineering, The Pennsylvania State University, University Park, Pennsylvania 16802, United States; Department of Physics, Karamanoglu Mehmet University, Karaman 70000, Turkey; orcid.org/0000-0002-3621-2481

Mikhail Chubarov – 2D Crystal Consortium-Materials Innovation Platform (2DCC-MIP), Materials Research

- Institute, The Pennsylvania State University, University Park, Pennsylvania 16802, United States; orcid.org/0000-0002-4722-0321
- Tanushree H. Choudhury 2D Crystal Consortium-Materials Innovation Platform (2DCC-MIP), Materials Research Institute, The Pennsylvania State University, University Park, Pennsylvania 16802, United States; orcid.org/0000-0002-0662-2594
- Saiphaneendra Bachu Department of Materials Science and Engineering, The Pennsylvania State University, University Park, Pennsylvania 16802, United States
- Leixin Miao Department of Materials Science and Engineering, The Pennsylvania State University, University Park, Pennsylvania 16802, United States
- Yuanxi Wang 2D Crystal Consortium-Materials Innovation Platform (2DCC-MIP), Materials Research Institute, The Pennsylvania State University, University Park, Pennsylvania 16802, United States; orcid.org/0000-0002-0659-1134
- Chenhao Qian Department of Materials Science and Engineering, The Pennsylvania State University, University Park, Pennsylvania 16802, United States
- Vincent H. Crespi 2D Crystal Consortium-Materials Innovation Platform (2DCC-MIP), Materials Research Institute, The Pennsylvania State University, University Park, Pennsylvania 16802, United States; Department of Physics, The Pennsylvania State University, University Park, Pennsylvania 16802, United States
- Joan M. Redwing Department of Materials Science and Engineering, The Pennsylvania State University, University Park, Pennsylvania 16802, United States; 2D Crystal Consortium-Materials Innovation Platform (2DCC-MIP), Materials Research Institute, The Pennsylvania State University, University Park, Pennsylvania 16802, United States; Occid.org/0000-0002-7906-452X
- Adri C. T. van Duin 2D Crystal Consortium-Materials Innovation Platform (2DCC-MIP), Materials Research Institute, The Pennsylvania State University, University Park, Pennsylvania 16802, United States; Department of Mechanical Engineering, The Pennsylvania State University, University Park, Pennsylvania 16802, United States;

 orcid.org/0000-0002-3478-4945

Complete contact information is available at: https://pubs.acs.org/10.1021/acs.nanolett.1c01517

Notes

The authors declare no competing financial interest.

ACKNOWLEDGMENTS

This work was financially supported by the National Science Foundation (NSF) through the Pennsylvania State University 2D Crystal Consortium—Materials Innovation Platform (2DCC-MIP) under NSF Cooperative Agreement DMR-1539916. D.R.H., S.B., and N.A. acknowledge support from the NSF CAREER Program (DMR-1654107) and the NSF Program EFRI 2-DARE (EFRI-1433378). This work utilized resources provided by the NSF-MRSEC-sponsored Materials Characterization Lab at Penn State (DMR-1420620).

REFERENCES

(1) Wang, Q. H.; Kalantar-Zadeh, K.; Kis, A.; Coleman, J. N.; Strano, M. S. Electronics and Optoelectronics of Two-Dimensional Transition Metal Dichalcogenides. *Nat. Nanotechnol.* **2012**, *7* (11), 699–712.

- (2) Wu, S.; Huang, C.; Aivazian, G.; Ross, J. S.; Cobden, D. H.; Xu, X. Vapor-Solid Growth of High Optical Quality MoS2 Monolayers with Near-Unity Valley Polarization. *ACS Nano* **2013**, 7 (3), 2768–2772
- (3) Zhu, Z. Y.; Cheng, Y. C.; Schwingenschlögl, U. Giant Spin-Orbit-Induced Spin Splitting in Two-Dimensional Transition-Metal Dichalcogenide Semiconductors. *Phys. Rev. B: Condens. Matter Mater. Phys.* **2011**, *84* (15), 1–5.
- (4) Palacios-Berraquero, C.; Kara, D. M.; Montblanch, A. R. P.; Barbone, M.; Latawiec, P.; Yoon, D.; Ott, A. K.; Loncar, M.; Ferrari, A. C.; Atatüre, M. Large-Scale Quantum-Emitter Arrays in Atomically Thin Semiconductors. *Nat. Commun.* **2017**, 8 (May), 1–6.
- (5) Das, S.; Gulotty, R.; Sumant, A. V.; Roelofs, A. All Two-Dimensional, Flexible, Transparent, and Thinnest Thin Film Transistor. *Nano Lett.* **2014**, *14* (5), 2861–2866.
- (6) Chhowalla, M.; Jena, D.; Zhang, H. Two-Dimensional Semiconductors for Transistors. *Nat. Rev.* **2016**, *1*, 16052.
- (7) Yoon, Y.; Ganapathi, K.; Salahuddin, S. How Good Can Monolayer MoS2 Transistors Be? *Nano Lett.* **2011**, *11* (9), 3768–3773.
- (8) Giannazzo, F.; Greco, G.; Roccaforte, F.; Sonde, S. S. Vertical Transistors Based on 2D Materials: Status and Prospects. *Crystals* **2018**, 8 (2), 70.
- (9) Najmaei, S.; Liu, Z.; Zhou, W.; Zou, X.; Shi, G.; Lei, S.; Yakobson, B. I.; Idrobo, J.-C.; Ajayan, P. M.; Lou, J. Vapour Phase Growth and Grain Boundary Structure of Molybdenum Disulphide Atomic Layers. *Nat. Mater.* **2013**, *12* (8), 754–759.
- (10) Kobayashi, Y.; Sasaki, S.; Mori, S.; Hibino, H.; Liu, Z.; Watanabe, K.; Taniguchi, T.; Suenaga, K.; Maniwa, Y.; Miyata, Y. Growth and Optical Properties of High-Quality Monolayer WS2 on Graphite. ACS Nano 2015, 9 (4), 4056–4063.
- (11) Huang, Y. L.; Ding, Z.; Zhang, W.; Chang, Y. H.; Shi, Y.; Li, L. J.; Song, Z.; Zheng, Y. J.; Chi, D.; Quek, S. Y.; et al. Gap States at Low-Angle Grain Boundaries in Monolayer Tungsten Diselenide. *Nano Lett.* **2016**, *16* (6), 3682–3688.
- (12) Zou, X.; Liu, Y.; Yakobson, B. I. Predicting Dislocations and Grain Boundaries in Two-Dimensional Metal-Disulfides from the First Principles. *Nano Lett.* **2013**, *13*, 253–258.
- (13) Ji, Q.; Kan, M.; Zhang, Y.; Guo, Y.; Ma, D.; Shi, J.; Sun, Q.; Chen, Q.; Zhang, Y.; Liu, Z. Unravelling Orientation Distribution and Merging Behavior of Monolayer MoS2 Domains on Sapphire. *Nano Lett.* **2015**, *15* (1), 198–205.
- (14) Cheng, J.; Jiang, T.; Ji, Q.; Zhang, Y.; Li, Z.; Shan, Y.; Zhang, Y.; Gong, X.; Liu, W.; Wu, S. Kinetic Nature of Grain Boundary Formation in As-Grown MoS2 Monolayers. *Adv. Mater.* **2015**, 27 (27), 4069–4074.
- (15) Majee, A. K.; Foss, C. J.; Aksamija, Z. Impact of Mismatch Angle on Electronic Transport Across Grain Boundaries and Interfaces in 2D Materials. *Sci. Rep.* **2017**, *7* (1), 1–13.
- (16) Kim, S. Y.; Kwak, J.; Ciobanu, C. V.; Kwon, S. Y. Recent Developments in Controlled Vapor-Phase Growth of 2D Group 6 Transition Metal Dichalcogenides. *Adv. Mater.* **2019**, *31* (20), 1804939.
- (17) Mak, K. F.; Lee, C.; Hone, J.; Shan, J.; Heinz, T. F. Atomically Thin MoS2: A New Direct-Gap Semiconductor. *Phys. Rev. Lett.* **2010**, 105 (13), 2–5.
- (18) Zhao, W.; Ghorannevis, Z.; Chu, L.; Toh, M.; Kloc, C.; Tan, P.-H.; Eda, G. Evolution of Electronic Structure in Atomically Thin Sheets of WS2 and WSe2. ACS Nano 2013, 7 (1), 791–797.
- (19) Kwon, Y.; Kim, K.; Kim, W.; Ryu, S.; Cheong, H. Variation of Photoluminescence Spectral Line Shape of Monolayer WS2. *Curr. Appl. Phys.* **2018**, *18* (8), 941–945.
- (20) Liu, B.; Fathi, M.; Chen, L.; Abbas, A.; Ma, Y.; Zhou, C. Chemical Vapor Deposition Growth of Monolayer WSe2 with Tunable Device Characteristics and Growth Mechanism Study. *ACS Nano* **2015**, *9* (6), 6119–6127.
- (21) Chen, W.; Zhao, J.; Zhang, J.; Gu, L.; Yang, Z.; Li, X.; Yu, H.; Zhu, X.; Yang, R.; Shi, D.; et al. Oxygen-Assisted Chemical Vapor

- Deposition Growth of Large Single-Crystal and High-Quality Monolayer MoS2. J. Am. Chem. Soc. 2015, 137 (50), 15632–15635. (22) Ji, H. G.; Lin, Y. C.; Nagashio, K.; Maruyama, M.; Solís-Fernández, P.; Sukma Aji, A.; Panchal, V.; Okada, S.; Suenaga, K.; Ago, H. Hydrogen-Assisted Epitaxial Growth of Monolayer Tungsten Disulfide and Seamless Grain Stitching. Chem. Mater. 2018, 30 (2), 403–411.
- (23) Kang, K.; Xie, S.; Huang, L.; Han, Y.; Huang, P. Y.; Mak, K. F.; Kim, C. J.; Muller, D.; Park, J. High-Mobility Three-Atom-Thick Semiconducting Films with Wafer-Scale Homogeneity. *Nature* **2015**, 520 (7549), 656–660.
- (24) Gao, Y.; Liu, Z.; Sun, D. M.; Huang, L.; Ma, L. P.; Yin, L. C.; Ma, T.; Zhang, Z.; Ma, X. L.; Peng, L. M.; et al. Large-Area Synthesis of High-Quality and Uniform Monolayer WS2 on Reusable Au Foils. *Nat. Commun.* **2015**, *6*, 8569.
- (25) Chiappe, D.; Ludwig, J.; Leonhardt, A.; El Kazzi, S.; Nalin Mehta, A.; Nuytten, T.; Celano, U.; Sutar, S.; Pourtois, G.; Caymax, M. Layer-Controlled Epitaxy of 2D Semiconductors: Bridging Nanoscale Phenomena to Wafer-Scale Uniformity. *Nanotechnology* **2018**, 29 (42), 425602.
- (26) Lan, C.; Zhou, Z.; Zhou, Z.; Li, C.; Shu, L.; Shen, L.; Li, D.; Dong, R.; Yip, S. P.; Ho, J. C. Wafer-Scale Synthesis of Monolayer WS2 for High-Performance Flexible Photodetectors by Enhanced Chemical Vapor Deposition. *Nano Res.* **2018**, *11* (6), 3371–3384.
- (27) Zhang, X.; Choudhury, T. H.; Chubarov, M.; Xiang, Y.; Jariwala, B.; Zhang, F.; Alem, N.; Wang, G. C.; Robinson, J. A.; Redwing, J. M. Diffusion-Controlled Epitaxy of Large Area Coalesced WSe2 Monolayers on Sapphire. *Nano Lett.* **2018**, *18* (2), 1049–1056.
- (28) Chen, J.; Shao, K.; Yang, W.; Tang, W.; Zhou, J.; He, Q.; Wu, Y.; Zhang, C.; Li, X.; Yang, X.; et al. Synthesis of Wafer-Scale Monolayer WS2 Crystals toward the Application in Integrated Electronic Devices. ACS Appl. Mater. Interfaces 2019, 11 (21), 19381–19387.
- (29) Chubarov, M.; Choudhury, T. H.; Reifsnyder Hickey, D.; Bachu, S.; Zhang, T.; Sebastian, A.; Bansal, A.; Zhu, H.; Trainor, N.; Das, S.; et al. Wafer-Scale Epitaxial Growth of Unidirectional WS2 Monolayers on Sapphire. *ACS Nano* **2021**, *15*, 2532–2541.
- (30) Yang, P.; Zhang, S.; Pan, S.; Tang, B.; Liang, Y.; Zhao, X.; Zhang, Z.; Shi, J.; Huan, Y.; Shi, Y.; et al. Epitaxial Growth of Centimeter-Scale Single-Crystal MoS2 Monolayer on Au(111). ACS Nano 2020, 14 (4), 5036–5045.
- (31) Reifsnyder Hickey, D.; Yilmaz, D. E.; Chubarov, M.; Bachu, S.; Choudhury, T. H.; Miao, L.; Qian, C.; Redwing, J. M.; van Duin, A. C. T.; Alem, N. Formation of Metal Vacancy Arrays in Coalesced WS2 Monolayer Films. 2D Mater. 2021, 8 (1), No. 011003.
- (32) Pulkin, A.; Yazyev, O. V. Spin- and Valley-Polarized Transport across Line Defects in Monolayer MoS2. *Phys. Rev. B: Condens. Matter Mater. Phys.* **2016**, 93 (4), 1–5.
- (33) Xiao, Y.; Zhou, M.; Zeng, M.; Fu, L. Atomic-Scale Structural Modification of 2D Materials. *Adv. Sci.* **2019**, 6 (5), 1801501.
- (34) Nakanishi, T.; Yoshida, S.; Murase, K.; Takeuchi, O.; Taniguchi, T.; Watanabe, K.; Shigekawa, H.; Kobayashi, Y.; Miyata, Y.; Shinohara, H.; et al. The Atomic and Electronic Structure of 0° and 60° Grain Boundaries in MoS2. *Front. Phys.* **2019**, 7 (MAR), 1–
- (35) Reifsnyder Hickey, D.; Wu, R. J.; Lee, J. S.; Azadani, J. G.; Grassi, R.; DC, M.; Wang, J. P.; Low, T.; Samarth, N.; Mkhoyan, K. A. Large-Scale Interlayer Rotations and Te Grain Boundaries in (Bi,Sb)2Te3 Thin Films. *Phys. Rev. Mater.* **2020**, *4* (1), 3–7.
- (36) Wang, S.; Rong, Y.; Fan, Y.; Pacios, M.; Bhaskaran, H.; He, K.; Warner, J. H. Shape Evolution of Monolayer MoS2 Crystals Grown by Chemical Vapor Deposition. *Chem. Mater.* **2014**, *26* (22), 6371–6379
- (37) Wang, X.; Gong, Y.; Shi, G.; Chow, W. L.; Keyshar, K.; Ye, G.; Vajtai, R.; Lou, J.; Liu, Z.; Ringe, E.; et al. Chemical Vapor Deposition Growth of Crystalline Monolayer MoSe2. *ACS Nano* **2014**, *8* (5), 5125–5131.
- (38) Chen, S.; Gao, J.; Srinivasan, B. M.; Zhang, G.; Sorkin, V.; Hariharaputran, R.; Zhang, Y. W. Origin of Ultrafast Growth of

- Monolayer WSe2 via Chemical Vapor Deposition. *npj Comput. Mater.* **2019**, 5 (1), 28 DOI: 10.1038/s41524-019-0167-2.
- (39) Dong, J.; Zhang, L.; Ding, F. Kinetics of Graphene and 2D Materials Growth. Adv. Mater. 2019, 31 (9), 1801583.
- (40) Cao, D.; Shen, T.; Liang, P.; Chen, X.; Shu, H. Role of Chemical Potential in Flake Shape and Edge Properties of Monolayer MoS2. *J. Phys. Chem. C* **2015**, *119* (8), 4294–4301.
- (41) Brivio, J.; Alexander, D. T. L.; Kis, A. Ripples and Layers in Ultrathin MoS2 Membranes. *Nano Lett.* **2011**, *11* (12), 5148–5153.
- (42) Wu, R. J.; Odlyzko, M. L.; Mkhoyan, K. A. Determining the Thickness of Atomically Thin MoS2 and WS2 in the TEM. *Ultramicroscopy* **2014**, *147*, 8–20.
- (43) Senftle, T. P.; Hong, S.; Islam, M. M.; Kylasa, S. B.; Zheng, Y.; Shin, Y. K.; Junkermeier, C.; Engel-Herbert, R.; Janik, M. J.; Aktulga, H. M.; et al. The ReaxFF Reactive Force-Field: Development, Applications and Future Directions. *npj Comput. Mater.* **2016**, *2*, 15011
- (44) Momeni, K.; Ji, Y.; Wang, Y.; Paul, S.; Neshani, S.; Yilmaz, D. E.; Shin, Y. K.; Zhang, D.; Jiang, J.-W.; Park, H. S.; et al. Multiscale Computational Understanding and Growth of 2D Materials: A Review. *npj Comput. Mater.* **2020**, *6* (1), 22.
- (45) Nayir, N.; Wang, Y.; Shabnam, S.; Miao, L.; Reifsnyder Hickey, D.; Zhang, X.; Bachu, S.; Alem, N.; Redwing, J. M.; Crespi, V. H.; et al. Modeling for Structural Engineering and Synthesis of Two-Dimensional WSe2 Using a Newly Developed ReaxFF Reactive Force Field. *J. Phys. Chem. C* **2020**, *124*, 28285–28297.
- (46) Komsa, H. P.; Kotakoski, J.; Kurasch, S.; Lehtinen, O.; Kaiser, U.; Krasheninnikov, A. V. Two-Dimensional Transition Metal Dichalcogenides under Electron Irradiation: Defect Production and Doping. *Phys. Rev. Lett.* **2012**, *109* (3), 1–5.
- (47) Komsa, H. P.; Kurasch, S.; Lehtinen, O.; Kaiser, U.; Krasheninnikov, A. V. From Point to Extended Defects in Two-Dimensional MoS2: Evolution of Atomic Structure under Electron Irradiation. *Phys. Rev. B: Condens. Matter Mater. Phys.* **2013**, 88 (3), 1–8.
- (48) Wang, S.; Lee, G. Do; Lee, S.; Yoon, E.; Warner, J. H. Detailed Atomic Reconstruction of Extended Line Defects in Monolayer MoS2. ACS Nano 2016, 10 (5), 5419–5430.
- (49) Lahiri, J.; Lin, Y.; Bozkurt, P.; Oleynik, I. I.; Batzill, M. An Extended Defect in Graphene as a Metallic Wire. *Nat. Nanotechnol.* **2010**, *5* (5), 326–329.
- (50) Chen, J. H.; Autès, G.; Alem, N.; Gargiulo, F.; Gautam, A.; Linck, M.; Kisielowski, C.; Yazyev, O. V.; Louie, S. G.; Zettl, A. Controlled Growth of a Line Defect in Graphene and Implications for Gate-Tunable Valley Filtering. *Phys. Rev. B: Condens. Matter Mater. Phys.* **2014**, 89 (12), 1–5.
- (51) Bets, K. V.; Artyukhov, V. I.; Yakobson, B. I. Kinetically Determined Shapes of Grain Boundaries in CVD Graphene. *arXiv* [cond-mat.mtrl-sci], 1412.4323, 2014. https://arxiv.org/abs/1412.4323 (accessed August 9, 2019).
- (52) van der Zande, A. M.; Huang, P. Y.; Chenet, D. a; Berkelbach, T. C.; You, Y.; Lee, G.-H.; Heinz, T. F.; Reichman, D. R.; Muller, D. a; Hone, J. C. Grains and Grain Boundaries in Highly Crystalline Monolayer Molybdenum Disulphide. *Nat. Mater.* **2013**, *12* (6), 554–561.
- (53) Wang, Z.; Ning, S.; Fujita, T.; Hirata, A.; Chen, M. Unveiling Three-Dimensional Stacking Sequences of 1T Phase MoS2 Monolayers by Electron Diffraction. *ACS Nano* **2016**, *10* (11), 10308–10316.
- (54) Sung, S. H.; Schnitzer, N.; Brown, L.; Park, J.; Hovden, R. Stacking, Strain, and Twist in 2D Materials Quantified by 3D Electron Diffraction. *Phys. Rev. Mater.* **2019**, *3*, No. 064003.
- (55) Ma, T.; Ren, W.; Zhang, X.; Liu, Z.; Gao, Y.; Yin, L. C.; Ma, X. L.; Ding, F.; Cheng, H. M. Edge-Controlled Growth and Kinetics of Single-Crystal Graphene Domains by Chemical Vapor Deposition. *Proc. Natl. Acad. Sci. U. S. A.* **2013**, *110* (51), 20386–20391.
- (56) Artyukhov, V. I.; Liu, Y.; Yakobson, B. I. Equilibrium at the Edge and Atomistic Mechanisms of Graphene Growth. *Proc. Natl. Acad. Sci. U. S. A.* **2012**, *109* (38), 15136–15140.

- (57) Ding, F.; Harutyunyan, A. R.; Yakobson, B. I. Dislocation Theory of Chirality-Controlled Nanotube Growth. *Proc. Natl. Acad. Sci. U. S. A.* **2009**, *106* (8), 2506–2509.
- (58) Chen, S.; Gao, J.; Srinivasan, B. M.; Zhang, G.; Sorkin, V.; Hariharaputran, R.; Zhang, Y. W. A Kinetic Monte Carlo Model for the Growth and Etching of Graphene during Chemical Vapor Deposition. *Carbon* **2019**, *146*, 399–405.
- (59) Li, X.; Dong, J.; Idrobo, J. C.; Puretzky, A. A.; Rouleau, C. M.; Geohegan, D. B.; Ding, F.; Xiao, K. Edge-Controlled Growth and Etching of Two-Dimensional GaSe Monolayers. *J. Am. Chem. Soc.* **2017**, *139* (1), 482–491.